THE UNIVERSITY of EDINBURGH

Edinburgh Research Explorer

Influence of fibre steering on the bearing performance of bolted joints in 3D printed pseudo-woven CFRP composites

Citation for published version:
Li, A, Zhang, H & Yang, D 2024, 'Influence of fibre steering on the bearing performance of bolted joints in 3D printed pseudo-woven CFRP composites', *Composites Part A: Applied Science and Manufacturing*, vol. 181, 108150. https://doi.org/10.1016/j.compositesa.2024.108150

Digital Object Identifier (DOI):
10.1016/j.compositesa.2024.108150

Link:
Link to publication record in Edinburgh Research Explorer

Document Version:
Peer reviewed version

Published In:
Composites Part A: Applied Science and Manufacturing

General rights
Copyright for the publications made accessible via the Edinburgh Research Explorer is retained by the author(s) and / or other copyright owners and it is a condition of accessing these publications that users recognise and abide by the legal requirements associated with these rights.

Take down policy
The University of Edinburgh has made every reasonable effort to ensure that Edinburgh Research Explorer content complies with UK legislation. If you believe that the public display of this file breaches copyright please contact openaccess@ed.ac.uk providing details, and we will remove access to the work immediately and investigate your claim.

Download date: 11. May. 2024

Influence of fibre steering on the bearing performance of bolted joints in 3D printed pseudo-woven CFRP composites

Aonan Li, Haoqi Zhang, Dongmin Yang*

School of Engineering, Institute for Materials and Processes, University of Edinburgh, EH9 3FB, Edinburgh, UK.

Abstract

Aiming to improve the bearing performance of bolted joints in carbon fibre reinforced polymer (CFRP) composites, this study investigates the impact of steered fibre paths around the hole edge within pseudo-woven (interlaced) composites that are manufactured by 3D printing. The influence of fibre steering on the crack initiation and propagation was examined through double-lap bearing tests performed on four distinct cases. Parallel to the comprehensive experimental study, digital image correlation (DIC) and X-ray computed microtomography (micro-CT) scans were performed to aid in understanding and identifying the various damage mechanisms in each specimen type. Results revealed that different patterns provided varying bearing abilities, with an employed pattern improving the initial bearing strength, initial fracture energy and ultimate fracture energy of the 3D printed pseudo-woven composite by 23.5%, 363.7% and 29.6%, respectively. Consequently, fibre steering in composites is found to be a promising method to tailor the bearing behaviour of bolted joints as required.

Keywords: CFRP; Bolted joints; Fibre steering; 3D printing.

* Corresponding author. Email: Dongmin.Yang@ed.ac.uk

1. Introduction

Carbon Fibre Reinforced Polymer (CFRP) is a composite material that exhibits superior specific strength and stiffness whilst maintaining a lightweight characteristic [1-4]. It finds extensive use in industries such as aerospace, automotive and construction to fulfil the demand for a high strength-to-weight ratio and rigidity [5-7]. In traditional manufacturing methods like autoclave and resin transfer moulding, continuous carbon fibres are typically arranged in a straight manner in each layer [8, 9]. In the field of structural engineering, bolted joints represent a highly efficient method for securing composite structures and facilitating load transfer within these assemblies. However, when mechanical fastening is required, through-holes are introduced by drilling processes, which result in the cutting of continuous carbon fibres and residual damage around the hole [10]. Consequently, the presence of holes in composites creates stress concentrations, posing a risk of early crack initiation and reducing the mechanical performance. The contact surface experiences micro-buckling when the fractured fibre is subjected to bearing loading, and delamination issues arise when through-thickness stress is applied to the surface. Therefore, composites with bolted joints tend to exhibit lower bearing stresses compared to their equivalent metal counterparts [11, 12].

To address the defects resulting from traditional machining processes, alternative manufacturing methods have emerged to produce composites with intricate geometries. Automated Tape Laying (ATL) and Automated Fibre Placement (AFP) techniques, for instance, allow for the creation of variable angle tow (VAT) composites with customised fibre paths [13]. Furthermore, additive manufacturing (AM), also known as 3D printing, has recently gained more attention. Compared to ATL and AFP, continuous fibre 3D printing offers greater design flexibility [14, 15]. This can be attributed to its higher

printing system resolution and the narrower width of the printed fibre tows (approximately 1-2 mm). In 2014, Markforged® introduced the first commercial continuous fibre printing system, which, supported by its dedicated software Eiger, employs a concentric approach to place fibres around geometrical singularities. Other researchers have also developed their own printers for continuous carbon fibre composites [16, 17], as well as optimised methods for continuous fibre placement. For example, a novel concept involved placing curved fibres along principal stress trajectories generated through finite element analysis (FEA) based on the loading conditions [18]. Innovative techniques have also been developed and evaluated for the fabrication of pseudo-woven composites integrated with features like notches[19, 20]. These advancements in fibre placement methods offer the possibility of printing composites with holes, thereby avoiding the strength losses commonly associated with conventional composite machining.

Numerous researchers have verified that the utilization of continuous carbon fibre in the field of 3D printing significantly enhances the mechanical properties of the produced parts [21-25]. This improvement undoubtedly extends to the domain of composite joints. Considering the fibre path design concepts, strategies such as the tensile principal stress path [26] and load path design [27] were proposed for the fibre placement within the composite joint. Fibres were tailored into layers and replaced the 0° layer as a reinforcement in composite laminates, thereby enhancing pin-load bearing strength. Fujii *et al*., [28] developed more precise and intricate composite bolted joints using 3D printing technologies, employing radially aligned straight fibres to resist compressive loads and circumferentially steered curvilinear fibres to withstand tensile and shear loads. Numerical modelling and experimental testing demonstrated that the bearing capacity of

specimens with curvilinear fibres surpassed that of conventional quasi-isotropic layup designs. Sugiyama, Matsuzaki [29] reinforced a composite bolt joint by varying the fibre volume fraction along the principal stress path, achieving increased stiffness and maximum load compared to samples with straight fibres. These studies focused on plates fabricated using fibre steering techniques to reinforce carbon fibre prepregs, although delamination occurred due to stiffness discontinuity and weak interlayer adhesion. The filament printing path, based on principal stresses, often contained sparse print paths, resulting in weak adhesion and non-uniform stiffness. Dickson and Dowling [30] produced a pseudo-woven laminate with a 6 mm diameter notch using 3D printing, demonstrating improved bearing strength compared to the mechanically drilled specimens. However, further investigation of more intricate fibre steering paths to form notches, rather than simple routing, could be explored to achieve exceptional bearing performance.

This paper presents a comprehensive experimental investigation of the influence of steered fibre paths on the bearing performance of 3D printed pseudo-woven composites with bolted joints subjected to double-lap shear loading. The composite specimens were manufactured using 3D printing techniques to locally tailor the fibre paths, followed by vacuum bagging-only curing and consolidation. Experimental tests were conducted while digital image correlation (DIC) analysis and X-ray computed micro-tomography (micro-CT) scanning were employed to analyse microscale properties such as fibre volume fraction, void content and crack propagation paths. The research aims to propose a novel design approach to enhance the bearing capacity of composite materials through fibre steering, while exploring the specific effects of this fibre steering method on the bearing performance of 3D-printed pseudo-woven composites.

2. Design and manufacturing

2.1 Fibre steering patterns in pseudo-woven composite

In previous work, 3D printing technique was applied to produce pseudo-woven laminates and the continuous fibres were diverted to leave the hole for bolted joints[30]. In this paper, the method of fibre interlacing was further developed and pseudo-woven patterns were customised to investigate the effect of fibre orientation change for bearing load transfer mechanism within the bolted composite joint.

The design concept aimed to maintain filament continuity, thereby enabling load transfer over an expanded area beyond the hole's edge. Fig. 1 illustrates the difference in how specific fibre tows (highlighted in black) were interlaced in each of the presented cases. Four cases were evaluated, including a mechanically drilled sample (case D) shown in Fig. 1 (a) for comparison, where all fibre paths remained linear and a through-hole was drilled. The other three cases, referred to as cases C, L, and U respectively, employed unique fibre steering patterns: squeeze-apart, diverted-away, and loop-back, as depicted in Fig. 1(b-d). In case C the filament path followed a similar approach to previous work [19] which was steered along the hole edge without altering the fibre orientation. Conversely, fibres were steered circularly around the edge in cases L and U, with orientation changes of 90 and 180 degrees respectively. Additional details about path planning can be found in Fig. A. 1.

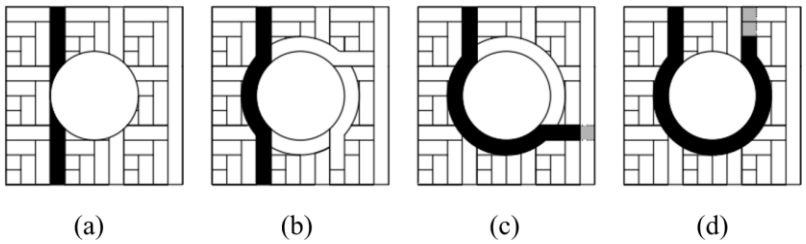

Fig. 1. Pseudo-woven pattern and fibre steering in (a) mechanically-drilled; (b) squeezed-apart; (c) diverted-away and (d) loop-back (Specific fibre unique to each case are marked in black, while interlaced part is depicted in grey).

2.2 3D printing and post-processing

In this study, a hybrid manufacturing process was employed, which involved 3D printing of composite preform layers followed by post-processing in the oven. The printing material stock was created using an in-house developed electrostatic powder deposition tapeline, similar to the method described in [30, 31]. Through this tapeline, 1k T300 carbon fibre tow sourced from Toray® was impregnated with powder-epoxy, resulting in the production of continuous filaments.

The composite filaments were 3D printed using a modified Prusa i3 MK3S printer, as illustrated in Fig. 2(a). The printer was interactively controlled via Pronterface, a comprehensive GUI host, connected through a USB interface. A passive continuous CF/epoxy filament feeding mechanism was employed, meaning that the feeding rate depended on the printing speed. The extruder and printing bed temperatures were set at 80 °C and room temperature, respectively. These temperature settings were chosen to ensure proper softening of the filaments within the nozzle and immediate cooling upon being printed on the bed, considering the weak adhesion between the printed tows and the bed. To prevent filament breakage caused by epoxy accumulation in the feeding channel, a polytetrafluoroethylene (PTFE) tube (Fig. 2 (b)) was inserted into the nozzle,

creating a smooth filament delivery process. The nozzle-to-bed distance was set at 0.1 mm, resulting in a printed tow width of approximately 1 mm. Since the filament consisted of continuous carbon fibres, a continuous printing path was generated using a Python script to achieve the desired pseudo-woven pattern. Selvedge regions (Fig. 2 (b)) were included in the print path for the purpose of path connection but were subsequently cut and removed, having no impact on the final specimen.

The connection design for the warp/weft filaments, as depicted in Fig. 2 (b), involved combining the steered filament pattern shown in Fig. 1 with the pseudo-woven units to form the bolt hole in each preform layer. Three types of connection patterns were designed and could be automatically selected and inserted into the G-code based on the filaments being connected. The first pattern, referred to as connection type I was a simple semi-circle used to connect adjacent same-direction filaments. The second pattern, identified as connection type II, was a three-quarter circle that enabled a smooth connection between warp and weft filaments. The connection methods for the third pattern varied based on the start and end points, as well as the layer dimensions. For the printing path in case L, for instance, the connection patterns were depicted as connection type III. The feed rate (also known as nozzle speed) was automatically determined by the Python program to achieve an efficient and stable printing process. Straight paths were assigned a rate of 400 mm/min, while curved paths were designated a slower rate of 200 mm/min to avoid filament detachment from the print bed. Following the 3D printing, curing and consolidation of the CF/epoxy preform was conducted through vacuum bagging in a stainless steel mould, a technique that has also been applied in other studies [32, 33]. To achieve a final specimen thickness of 3mm, the number of layers was intentionally set at 13. These layers were subsequently integrated using a compression

mould. The components of the mould and vacuum bagging setup are shown in Fig. 2 (c). As illustrated, to facilitate subsequent demoulding, this mould was designed comprising upper and lower plates, as well as lateral plates as its principal components. To directly form holes of specified dimensions during the vacuum bagging process, thereby avoiding the damage to composite components that mechanical drilling can induce, a forming pin with a diameter of 6mm was employed. It was fixed to the lower plate and, during the extrusion moulding process, aligned with a through-hole track reserved in the upper plate. The entire mould will be aligned and secured through the use of positioning pins and fixing bolts, ensuring the compression movement is limited and the lateral plates are fixed during vacuum bagging process. Before assembly, all components were coated with CR1 easy-lease chemical release agent. The mould was then covered in breather fabric to absorb the epoxy that had leaked out and was entirely packed in vacuum bagging films. A vacuum pump was used to create a vacuum environment, providing the necessary vacuum pressure for shaping. For details on the changes within the mould during the melting and curing process, view Fig. 2 (d).

The temperature cycle curve for this process is illustrated in Fig. 2 (d). A temperature gap between the melting phase (around 40-60 °C) and the curing phase (above 150 °C) was present for the powder epoxy. As a result, excess epoxy and voids were squeezed out, leading to a high fibre volume fraction. To ensure easy removal of the cured sample from the mould, a non-stick PTFE sheet was applied around the mould, and the entire mould was coated with a release agent. The mould was then covered with a breathable fabric to absorb any excess melted epoxy, vacuum-packed, and placed in an oven. The heating process consisted of three stages: the oven temperature initially reached 40 °C and remained for 6 hours to eliminate moisture; it was then raised to 120 °C to melt the epoxy;

Finally, the temperature was further increased to 180 °C and held for 2 hours to ensure proper consolidation and subsequent curing of the lay-up preform. The quality and dimensions of the specimen bolt holes, formed either by mechanical drilling or co-cure, are summerized in Fig. A. 2.

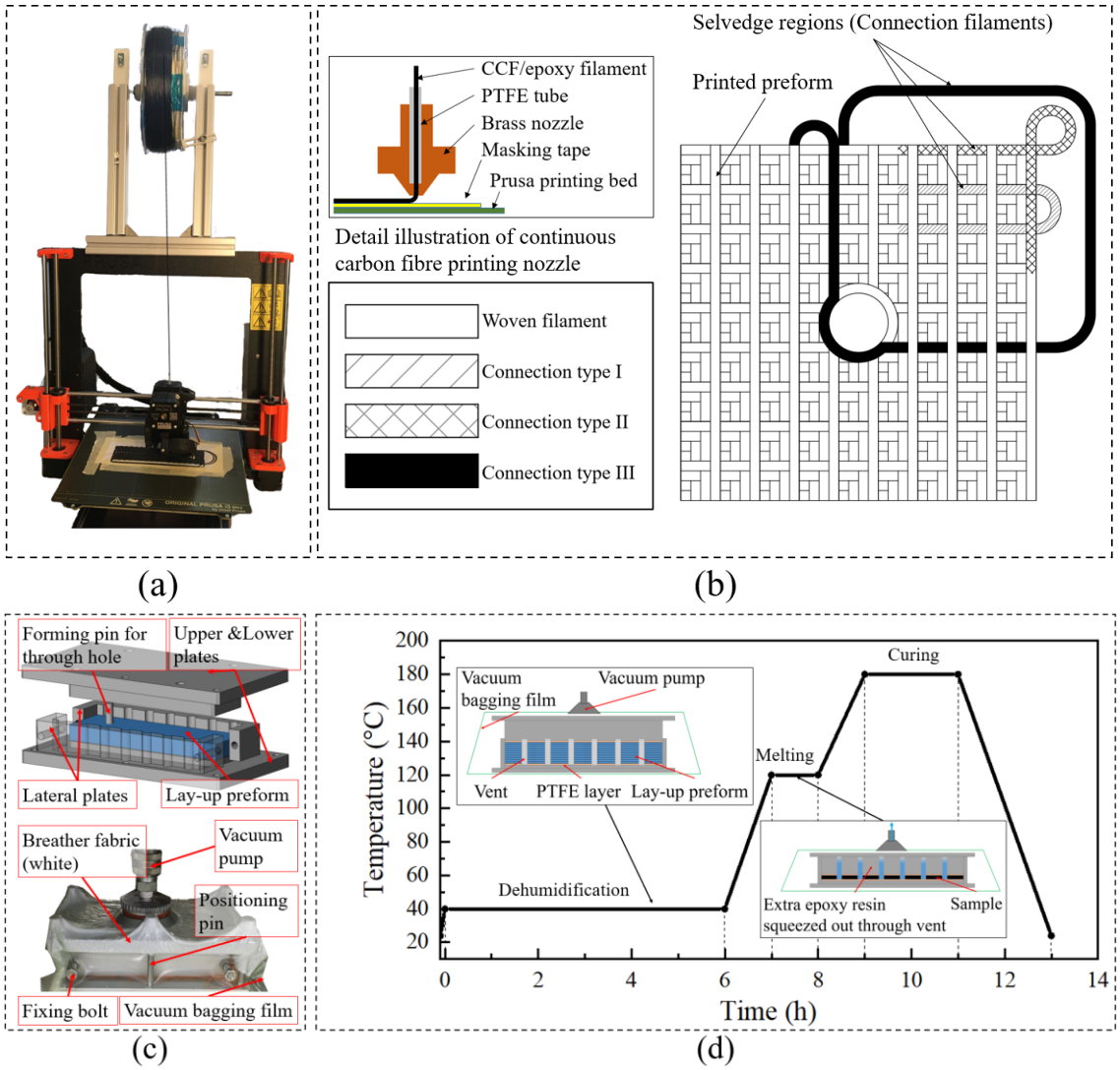

Fig. 2. (a) Prusa i3 MK3S printer; (b) Connection of adjacent paths for continuous printing; (c) Components of the mould and vacuum bagging setup; (d) Heat cycling of oven curing.

3. Mechanical testing and Micro-CT characterisation

In this study, the ASTM D5961 standard was followed to conduct experimental tests focusing on the bearing response of fastened joints in multi-directional polymer matrix composite laminates reinforced by high-modulus fibres. The chosen testing method was the double lap joint configuration (Procedure A in the standard). The experimental work was performed using an MTS Criterion C45.305 electromechanical load frame equipped with a sturdy 300 kN load cell (as shown in Fig. 3). For the MTS machine, its load cell capacity was calibrated to just 3% of full scale through its accompanying software, TW elite, to ensure more accurate measurement results. To ensure appropriate failure timing within the recommended range of 1 to 10 minutes, a loading rate of 0.5 mm/min was employed in all tests, in accordance with the ASTM standard. The specimens were securely positioned within a robust steel fixture fastened with a steel bolt and washers (as depicted in Fig. 3). The bolt type is a nut type, made from A2 304 stainless steel. Both the bolt and nut were selected to prevent yielding at the maximum applied force, as the type of fastener is not a variable under test in this study. The bolt features a hex head, and to ensure that thread damage does not introduce additional variables, the unthreaded shank length is specified to be 13 mm. Moreover, as there will be no deformation or damage to the bolt throughout the experimental process, it is reused to maintain consistency in the variables. Four A2 304 stainless steel plain M6 washers, with an outer diameter of 13mm and a thickness of 2mm, are used. These washers are located between the fixture loading plate and the specimen, between the bolt head and the fixture loading plate, and between the nut and the fixture loading plate. The bolts used have a specific diameter of 5.97mm. According to the specimen data in Fig. A. 2, even though there is some clearance between the bolt and certain composite specimens, it is within the

tolerance range allowed by the ASTM standard (+0.075/-0mm). The nut was carefully tightened to a torque of 3 N·m using a torque wrench. A 0.5 kN preload was applied to each sample prior to testing, and two specimens were tested for each fibre path pattern.

Allied Vision Manta G-146 camera with Canon EF-S 18-55mm f/3.5-5.6 IS II lens was adopted, functioning as a visual extensometer, recording the displacement in the tests at a specific location as depicted in Fig. 3. The maximum resolution of the camera was 1,360 x 1,024 pixels and lens was 18–55 mm f/3.5–5.6. The rate of data acquisition remained stable at 10.02 measurements per second, with a margin of error of ± 0.02.

Additionally, to investigate the influence of fibre steering on strain propagation prior to initial failure, extra tests were conducted for each case using Procedure C, a test method demonstrated in the ASTM D5961 standard. Procedure C tests provide a more detailed understanding of deformation and strain distributions near the bolt hole through DIC analysis, which cannot be obtained in procedure A due to the obstructed view caused by the steel fixture. The focus was on the strain distribution before the initial failure as the loading conditions in both 'Procedure A' and 'Procedure C' were identical during the elastic stage. One specimen from each fibre steering case was subjected to procedure C tests, and the detailed experimental setup of procedure C can be seen in Fig. A. 3. The strain distribution was recorded precisely half a minute into the experiment, a stage where all four cases remained within the elastic phase and subjected to a longitudinal tensile deformation of 0.25 mm.

The DIC analysis was conducted utilising Ncorr v1.2, a comprehensive open-source 2D DIC MATLAB programme [34]. Initially, videos recorded by the high-speed camera were converted into images using a video-to-JPG converter, extracting images at a rate

of one image per second from the video. Subsequently, all images were uploaded into Ncorr. Within this set, the image captured before loading on the test machine serves as the reference image. After uploading the images, the region of interest (ROI) was drawn along the contours of the bolt and the contour of the sample. This delimitation facilitated the extraction and calculation of the strain distribution exclusively around the hole in the composite. The magnitude of displacement in the images was determined by pre-setting the value of units per pixel. In this study, the unit was set to millimetres, with the ratio derived from the actual width of the specimen, which was 36mm. Consequently, Ncorr can estimate the displacement in other areas, thereby calculating the strain distribution throughout the loading process. Furthermore, the Y-direction was defined as the loading direction, and the X-direction was the in-plane width direction of the specimen. Therefore, the software plots Exy, representing the shear strain distribution in the plane direction of the specimen.

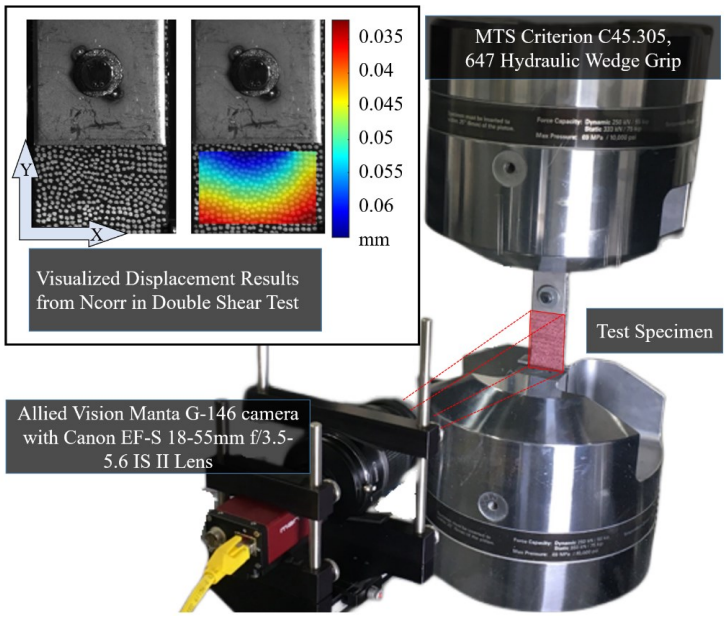

Fig. 3. The experimental set-up for double-lap shear bearing test.

To gain a clearer view of the cracks within the composite, micro-CT scans were conducted at the in-house developed micro-CT facility in the Grant Institute, School of Geosciences, the University of Edinburgh (shown in Fig. 4). To achieve better resolution (around 10 μm pixel size), the tested specimens were cut into small pieces of approximately the same size with around 10 mm in width. The X-ray scans were performed with an accelerating voltage of 70 kV and a power of 24 W. The exposure time was set to 2 seconds to obtain high-quality images in terms of contrast and intensity. The raw scan data were reconstructed using Octopus 8.9 in LabView®, and the threshold value for image analysis was determined based on expertise. Through micro-CT imaging, the crack propagation within the specimens caused by bearing load was successfully captured. The commercial software Avizo was utilized for 3D visualisation and analysis, particularly its volume rendering capabilities, which enabled the identification of crack propagation and material deformation at any location within the scanned specimen.

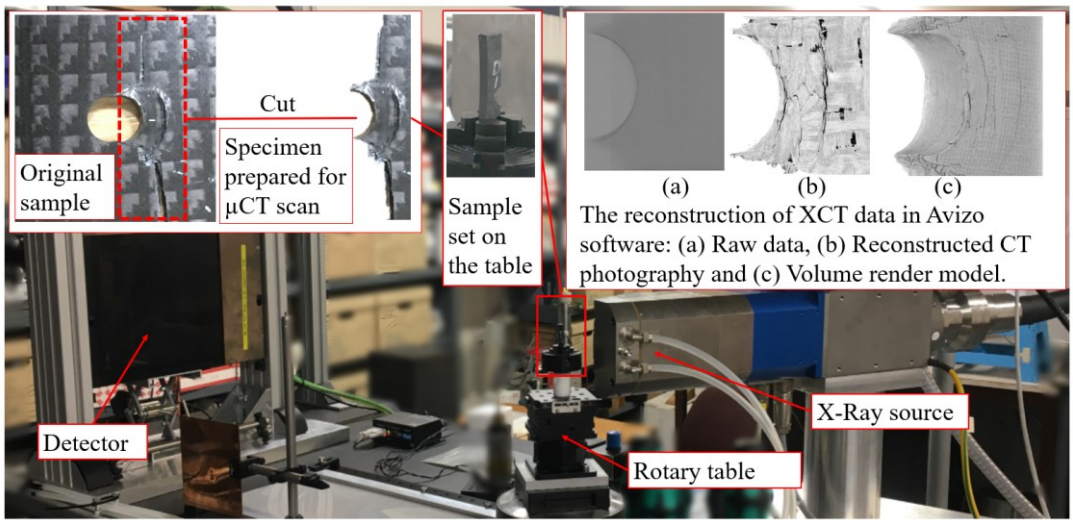

Fig. 4. Micro-CT scan set-up and the reconstruction of 3D images in Avizo software.

4. Results and discussion

In this section, the bearing performance of 3D printed pseudo-woven composites under double lap shear loading was analysed, integrating the findings from both experimental

and visual studies. Initially, the analytical results for each case are individually detailed in Fig. 5-8, including the elastic and plastic deformation, failure pattern and crack propagation identification. Subsequently, Fig. 9 summarises the experimental results to evaluate the capability of each pattern.

4.1 Analysis of elastic response, failure mode and crack propagation

Figs. 5-8 depict (a) the load-displacement curves for the four cases, which are annotated with numerical markers to represent different stages: from point ① to ② denoting the elastic stage, from point ② to ③ indicating plastic deformation, and point ③ representing the ultimate failure point. These curves are accompanied by DIC imagery and a post-failure macroscopic photograph, with damage types highlighted; (b) 3D reconstructed micro-CT image with labelled crack propagation; sliced micro-CT images viewed in the (c) transverse direction and (d) thickness direction. Here only the necessary slices are shown and cracks are highlighted with colour associated with the labelled cracks in the 3D model. Together, these images offer further insights into the different failure modes observed during various loading periods.

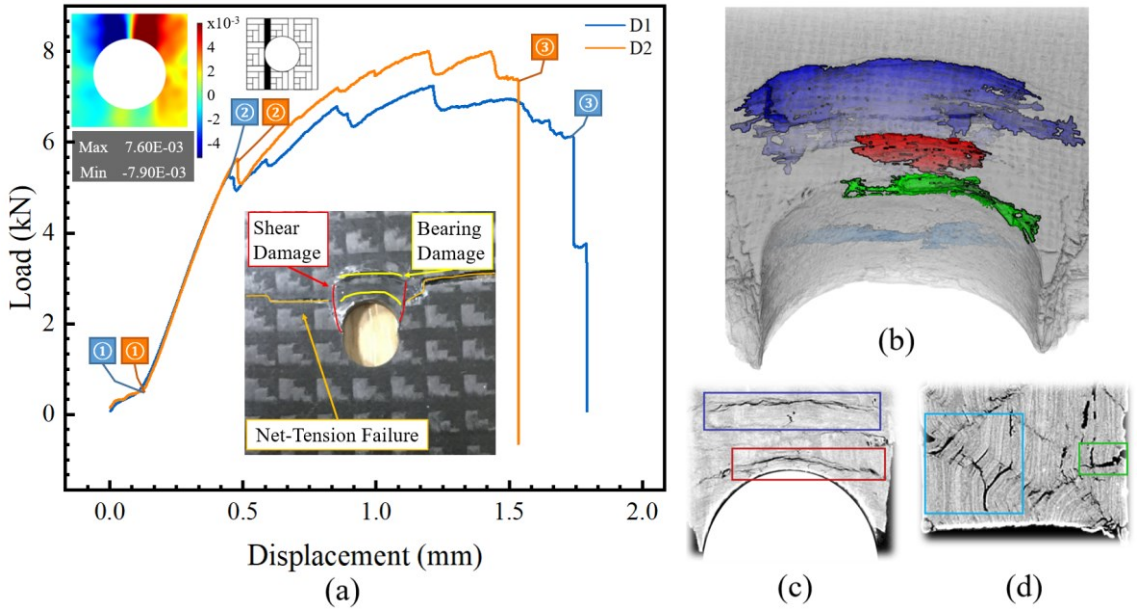

Fig. 5. Load-displacement curve and visual analysis results for case D.

As shown in the curve in Fig. 5, the joints exhibit structural nonlinearity with minor initial displacements until the bolt attains complete intimate contact with the hole at approximately 0.5 kN (point ①), subsequently followed by a linear correlation up to around 5.4 kN. From the DIC image, the distribution of shear strain in case D reveals the location of the highest concentration at the edge of the hole. This indicates a probable initiation point for shear deformation at this location. After a linear load increase during the elastic phase a sharp load drop (point ②) occurs. Beyond this drop, a combination of shear and bearing-induced progressive damage mechanisms was observed, extending from point ② to point ③, characterised by alternating phases of load increase and sharp decrease, a pattern that repeated until ultimate tension failure (point ③). This nonlinear behaviour is evidenced in the macroscopic photograph, which shows the shear cracks from the edge of the hole and subsequent bearing-induced crushing. Moreover, the CT image highlights cracks indicative of bearing load sustained solely by the direct contact area, leading to further kinking and crush failure as seen in the micro-CT slices (Fig. 5(b), (d)). in the context of case D, the initial load drop represents a significant disadvantage for the joint's overall load-bearing capacity. Despite the specimens' capability to continue carrying load, their stiffness gradually decreases. This is due to the propagation of the shear crack reducing the effective area bearing the load, leading to a weakened load transfer ability and worsened stress concentration. Overall, the above failure mechanism

is considered to be particularly prevalent in mechanically drilled composite joints, because only the direct contact region bears the load without any load transfer.

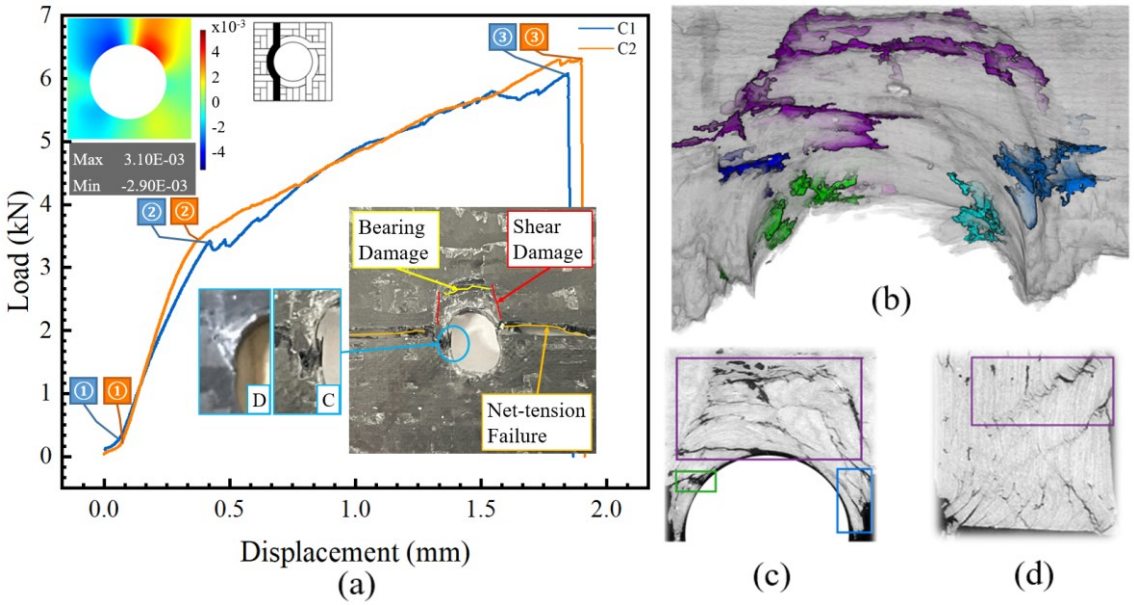

Fig. 6. Load-displacement curve and visual analysis results for case C.

From the photograph shown in Fig. 6 (a), a similar post-failure macroscopic photograph with case D could be seen in case C, but with differences in the specifics of the failure. Starting from the elastic phase (point ①), the strain distribution in case C indicates a reduced strain concentration, as evidenced by a lower value. This suggests that the steered continuous fibres were successful in transferring load from the hole edge to a larger area. The consequential enhancement in shear resistance can be substantiated by the load-displacement curve, as C1 exhibits a less steep drop in load (from point ② to point ③) compared to case D, and C2 even demonstrates no initial sharp load drop at the inception of plastic deformation. By observing the fracture surface around the hole edge and cracks shown in the slices in Fig. 6 (b) and (c), although shear cracks were initiated, they did not trigger significant shear damage propagation in the first place until continuous fibres around the edge failed (highlighted with green and cyan).

In addition, the bearing resistance was also enhanced as the bolt movement induced a gradual increase in load without an obvious sharp drop. This signifies that not only was the region directly in contact with the bolt bearing the load, but the continuous fibres were also under tension to provide support. This observation is further validated by the macroscopic photography outlined, where the crack is seen at the neck of the hole instead of the corners, as observed in case D. Also from the micro-CT slices, instead of severe kinking, only minor crushing around the bearing region was identified.

Despite its contributions to bearing resistance, the steered fibre path C is not perceived as an efficient load transfer mechanism, because of the early initial deformation (point ②). A difference was observed between the response curves of specimens C1 and C2. Specifically, specimen C1 exhibited sharp load drops, whereas the curve for C2 demonstrated a smooth load-deflection behaviour. This observation suggests that shear and bearing-induced progressive damage continue to be the principal drivers of nonlinear behaviour in case C. The specific nature of the nonlinearity is determined by whether bearing or shear damage is the predominant initial mechanism. This uncertainty complicates its applicability. Also, the crack, attributed to this initial failure, reduced the bearing region capable of supporting the load from the bolt, as further confirmed by the crack marked with purple in the micro-CT scan image (Fig. 6 (c)), resulting in a significant stiffness loss.

Based on the results, while the steered fibre path in case C seems to enhance both shear and bearing resistance, it still fails to serve as an efficient load transfer mechanism. This inefficiency primarily stems from the early initial deformation and stiffness loss due to the subsequent cracking.

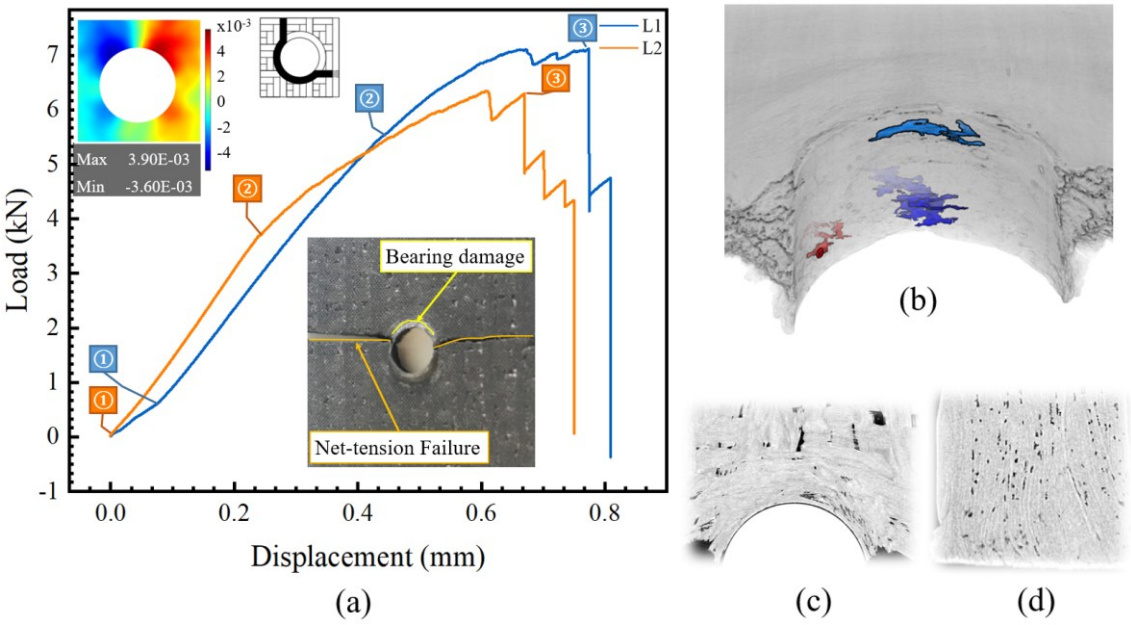

Fig. 7. Load-displacement curve and visual analysis results for case L.

In case L, the load transfer effect facilitated by the steered fibres becomes apparent from the shear strain distribution. The distribution of shear strain moved to a larger area beyond the hole edge, although some concentration remains. The load-displacement curves for case L (Fig. 7) display a linear behaviour until the stiffness degradation occurs at point ②. Subsequent damage emerged at the edge of the hole, with the specimen's stiffness progressively and smoothly decreasing alongside bolt movement. No severe shear damage could be identified, either from photography or from the CT images. In this case, the specifically steered fibres were to be part of the warp and then transition into the weft. This fibre path design improved the shear resistance of the composite by altering the fibre orientation and providing a less direct path for the shear crack to initiate along the length of the fibres, potentially enhancing damage tolerance. However, a prolonged damage accumulation stage was absent before final tension failure, suggesting that while fibres steered in the L path ensured stable stiffness, they might also make the area around the hole more brittle. Upon reaching maximum load, the specimens failed abruptly in tension

(point ③), accompanied by a series of sharp drops, and the load quickly decreased to zero. This implies that the orientation change potentially creates a weak point in the composite structure and the efficiency of tensile load transfer might be compromised at this junction, possibly leading to a decrease in the composite's tensile strength. The micro-CT result supports this assertion as it shows rarely bearing damage and from the photograph, the cracks initiated precisely at the fibre inflection point. In conclusion, the L pattern could enhance shear resistance and bearing resistance by transferring the load. However, the turning point of the path caused stress concentration and resulted in a weak point in terms of tension. This makes the joint to be more prone to brittle tensile failure.

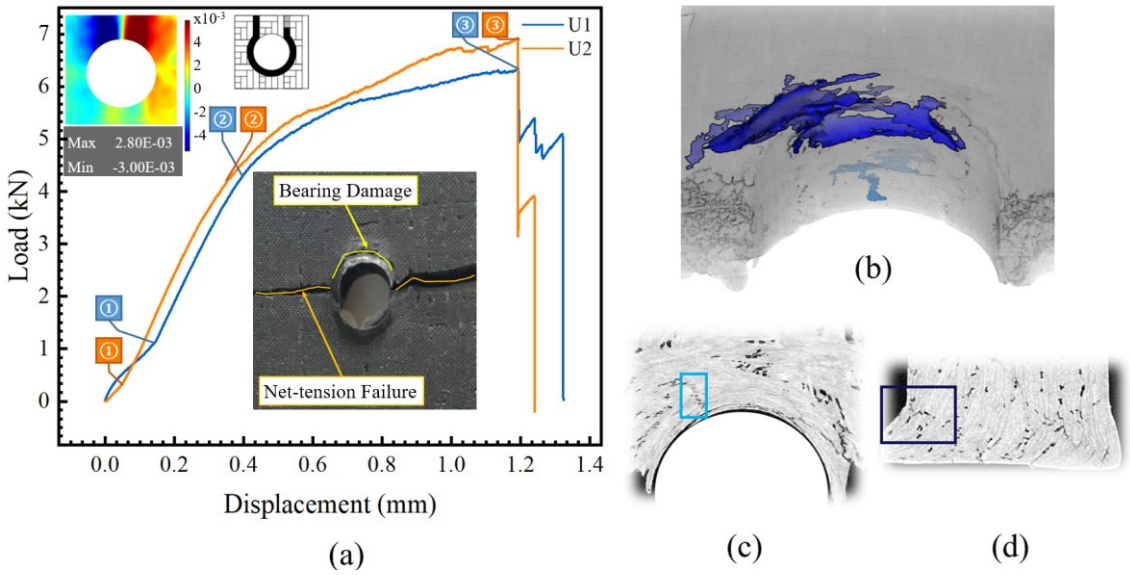

Fig. 8. Load-displacement curve and visual analysis results for case U.

For case U, the DIC image reveals that the fibre layout effectively minimised strain concentration around the hole edge and, therefore, helps resist the initiation and propagation of cracks. The load-displacement curves presented in Fig. 8 corroborate this improvement. Contrary to the sharp drops observed in other cases, case U displays a smoother, more gradual decline (from point ② to point ③), suggesting a more evenly distributed non-linear process within the composite rather than being localised in a few

high-strain regions. The ability to alleviate shear strain concentration in a composite joint reflects the joint's resistance to localised deformation, which contributes to its overall mechanical performance with higher IPB strength and IF energy. This could be obviously seen from the load-displacement curve without a sharp load drop during the plastic deformation phase. Moreover, even though the bearing resistance in case U does not quite align with that in case L, as reflected by the reduction in stiffness, a prolonged damage accumulation stage appeared before the final tension failure. This can indicate an enhanced fracture toughness which is critical for the performance and longevity of composite structures across various applications.

The load transfer mechanism in this pattern is considered the reason for the toughness improvement. Unlike the L path, there was no inherent weakness prompting early brittle failure along the fibres. Also, the steered fibres in case U distribute the bolt’s bearing force along their length, in conjunction with the direct contact region, providing a level of bearing resistance. Thus, a better balance was achieved between brittleness and energy absorption by this pattern, resulting in smooth progressive damage mechanisms. The post-failure photography and micro-CT results reveal that bearing damage mainly occurs at the direct contact surface. And the final catastrophic tension failure due to the breakage of the steered fibres happened at the neck of the hole which is reasonably the structurally weakest point.

In conclusion, the steered U fibre path provides the bolted joint with an improved better load transfer mechanism ensuring no significant shear strain concentration occurs and an ability to resist crack initiation and propagation. All these improvements lead to a uniform failure process, enhancing the composite’s overall performance.

4.2 Comprehensive evaluation of mechanical performance

This section begins with a comparative analysis of the performance of all four composite bolted joints, taking into account five mechanical properties. By comparing and contrasting these characteristics, the relative advantages and limitations of each fibre steering type are revealed. This analysis serves as a crucial step towards the selection and design of optimal composite joints, aligning with the specific demands and constraints of the intended application.

In the following discussion, a brief explanation of key parameters will be presented. In this study, the bearing chord (BC) stiffness was calculated between 50 MPa and 150 MPa. This property reflects the bearing resistance capacity during the elastic phase. Initial peak bearing (IPB) strength was selected to characterise the joint's resistance against initial cracking and was identified by a sharp drop in the bearing stress. At this point, IPB strength and initial fracture (IF) energy were obtained for comparison. Upon reaching maximum force, ultimate bearing (UB) strength and ultimate fracture (UF) energy were recorded to demonstrate the maximum capability of a bearing specimen. The selection and computation of data were carried out using Origin 2021b, a software for data analysis and graphing. A summary of these parameters is presented in Fig. 9 and their respective definitions and calculation equations are detailed in Fig. A. 4 and Eq. (A.1)- Eq. (A.3) of the appendix.

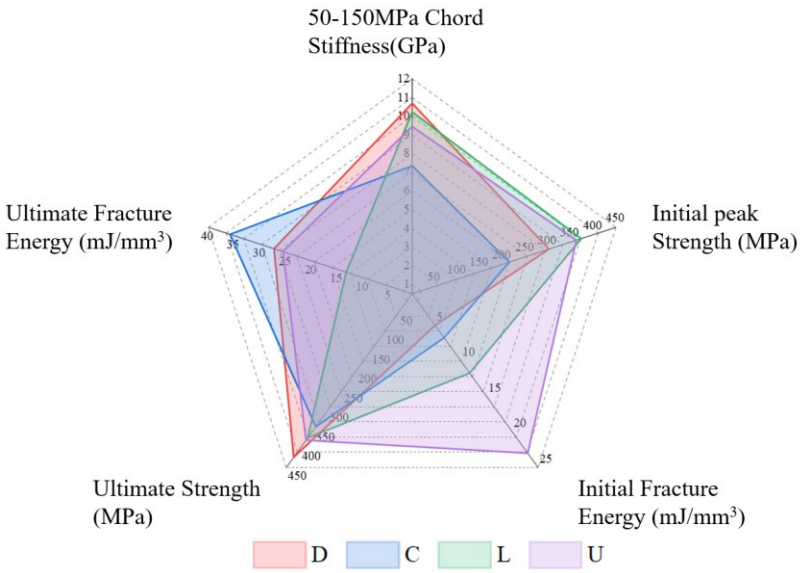

Fig. 9. Comparative analysis of four cases based on mechanical properties.

For the elastic phase, in terms of 50-150 MPa BC stiffness, all the fibre-steered cases exhibited values that were lower compared to case D. This was primarily attributed to the higher porosity within the fibre steering patterns cases caused by the manufacturing method mentioned in section 2. For these cases, a pin was used to form a hole during the vacuum bagging process, thereby providing an exit for air during compression. Consequently, the extruded voids were more likely to remain around the bolt hole in fibre-steered cases. In case D, the formation of holes differs as no pin is required and holes are drilled at specified locations after vacuum bagging process. Voids and porosity are recognised as significantly detrimental defects within composite materials, extensively investigated due to their adverse effects on mechanical integrity [35-38]. These imperfections notably compromise various mechanical properties including longitudinal compressive modulus and strength, transverse tensile modulus and strength, alongside bending and shear characteristics [39-42]. This assertion was substantiated by porosity calculations carried out using Avizo with results presented in Table A.1 indicating that the porosity in fibre-steered cases is nearly double that of drilled ones. This illuminates

the observed discrepancy in BC stiffness. Additionally, matrix crushing is more prone to occur as voids converge into microcracks during testing. However, a comparison of the IPB strength values from Fig. 9 reveals that only case C exhibits a lower value, suggesting that while defects introduced during the manufacturing process may compromise the matrix's mechanical properties. The steered fibre patterns in cases L and U still benefited the entire joints bearing performance, as joints were not significantly affected in terms of initial peak bearing damage. Therefore, future improvements in the manufacturing process could potentially further enhance the performance of the fibre steered cases.

Additionally, among the fibre-steered cases, different steering patterns contributed variably to deformation resistance. With the lowest BC stiffness in case C, the squeezed-apart pattern is relatively weaker than diverted-away and loop-back, of which the stiffness increased by 39.25% and 28.60% separately. As discussed earlier, the deformation resistance ability depends on how well it reduces strain concentration caused by the bolt and this relies on the effectiveness of the load transfer mechanism. Compared with case D, in terms of the IPB strengths, an improvement (23.5% and 20.0% increase respectively in cases L and U) was observed in the fibre-steered cases, with the notable exception of case C. As previously discussed, the shear damage will cause a sharp load drop, and this type of initial failure was exclusively observed in case D and case C, leading to a low IPB strength. This difference is mainly attributed to the fact that, in case L and case U, altering the fibre direction around the bolt-hole edge prevents shear crack from initiating and propagating along the length of the fibres. This enhancement in shear damage tolerance is corroborated by the load-displacement curves, macroscopic photographs, and micro-CT slices. In these characterisations, no occurrence of shear damage was observed, as discussed in Section 4.2. This reduces the risk of shear failure at the very beginning.

However, in situations like case C where the fibre direction remains unchanged, the steered continuous fibre only mitigates the plastic deformation caused by shear stresses without completely preventing it.

In addition, the early onset of shear damage in both cases C and D compromises their ability to absorb IF energy. In comparison with case D, case L exhibits an increase in energy absorption by 135.8%, attributed to its high IPB strength. However, an abrupt failure was observed in case L, leading to an energy absorption lower than that of case U. The joint in case U is considered superior among other cases, absorbing about 363.7% higher energy, achieved through a more progressive, less catastrophic deformation process.

Up to this point in the discussion, it can be asserted that the U pattern achieved a better initial failure tolerance in the composite bolted joint by possessing a higher IPB strength and IF energy. The steered fibre not only provides high resistance to shear cracking but also ensures there are no induced weaknesses that could compromise tension resistance. As conventional CFRP composites are not widely utilised as energy absorption components due to their complex energy absorption mechanisms [43-45], the improvement of IPB strength and IF energy could significantly broaden the potential applications for CFRP composites.

In order to gain a deeper insight, the UB strength and UF energy of each case were also compared. This comparison primarily aims to provide valuable insights for future studies that focus on reinforcing areas beyond the hole edge using fibre steering. From Fig. 9, none of the fibre-steering cases outperformed the UB strength achieved by the drilled case. For case D, after the initial load drop, the initial shear damage did not lead to final

brittle shear out failure and the bearing damage occurred due to the high edge distance ratio of the sample, which helped case D to reach a better ultimate ability. However, compared to case D, case C exhibited a 29.6% increase in UF energy. With substantial stiffness loss following the initial damage, the joint in case C experienced gradual bearing damage, allowing it to absorb more damage before ultimate failure. For the other two steered fibre cases, they mitigated the strain and stress concentrations at the edge of the bolt hole, but the region beyond the hole was unchanged leading to low UB strength and UF energy. Although the improvements presented here are specific to the initial failure stage, the ultimate goal is to optimise all stages of joint behaviour to ensure structural integrity during the entire bearing period. These findings contribute to guiding future research towards achieving this goal.

After evaluating all the properties, it is found that reinforcing the edge of the hole with steered fibre significantly enhanced the initial stages of failure for the bolted composite joint. Even though the steered fibre pattern implemented in this study did not significantly increase the ultimate capacity, a comprehensive analysis of the radar chart in Fig. 9, indicates that case U exhibited the most balanced bearing performance throughout the entire bolt bearing process.

5. Conclusions

The effect of fibre steering on the crack initiation and propagation was examined through double-lap bearing tests performed on four distinct cases and various damage mechanisms were studied in all the cases. The possibility of enhancing the joint's bearing performance by fibre steering was explored. Based on the results, the following conclusions can be drawn.

- Fibre steering can address the issue of shear strain concentration at the edge of the bolt hole by maintaining the continuity of the carbon fibre. It transfers the bearing load into a larger volume of material. Furthermore, altering the fibre orientation enhances the load transfer mechanism's effectiveness. For pseudo-woven composites, an orientation change of 180 degrees has been proven to distribute strain evenly and reduce the maximum absolute strain value by approximately half.
- Regarding the enhancement of initial damage toughness, merely maintaining carbon fibre continuity is insufficient. This is because both shear and bearing damage will still commence. By adjusting the orientation of the steered fibre around the hole edge, the initiation and propagation of shear cracks along the fibre direction become less likely. This finding is clearly demonstrated in case U, where notable enhancements of IBP strength and IF energy were observed, with improvements approximating 23.5% and 363.7% respectively.
- The steered fibre provides different bearing ductility for the composite joint, depending on the degree of fibre orientation change. According to this study, a change of 90 degrees induces brittleness, while 180 degrees enhances ductility. Therefore, fibre steering emerges as a potential solution for meeting specific bearing requirements by manipulating the fibre path.
- Steering fibres only around the hole edge may not improve ultimate toughness and might even weaken it. Future studies should focus on optimising load transfer with steered fibres considering the entire structure.
- Based on the discussions in Section 4.2, the fibre steering technique enables the tailoring of composite structures with varying performances dependent on the

steered pattern. For instance, this method can orient composite materials towards enhanced strength (the optimal initial peak strength observed in case L), increased energy absorption (the best ultimate fracture energy seen in case C), or a more balanced capability (illustrated by case U in Fig. 9) to meet specific application requirements. This level of customisation surpasses what is achievable with conventional composites, presenting new potential for composite materials in industries like aerospace, where the ability to customise material properties for specific performance requirements can lead to significant improvements in aircraft design and functionality.

The absence of comprehensive data on the progressive failure process limits the research into the exact mechanisms by which the specific steered fibres transfer the load. Further simulation studies will be conducted to investigate these aspects. Additionally, to enhance the understanding of the fibre-steered composite joint's performance comprehensively, future work will necessitate extensive testing and evaluation. This includes areas such as fatigue, bolt-hole clearance, torque, bolt type, single lap configurations, and composite-to-composite interactions.

Acknowledgements

The authors gratefully appreciate the Institute for Condensed Matter Physics and Complex Systems at the University of Edinburgh for Avizo software used in this research project.

CRediT authorship contribution statement

Aonan Li: Data curation, Methodology, Software, Visualization, Writing – original draft. **Haoqi Zhang:** Methodology, Software, Writing – review & editing. **Dongmin Yang:** Conceptualization, Investigation, Writing – review & editing, Project administration, Supervision.

Declaration of Competing Interest

The authors declare that they have no known competing financial interests or personal relationships that could have appeared to influence the work reported in this paper.

Appendix A. Supplementary data and explanation

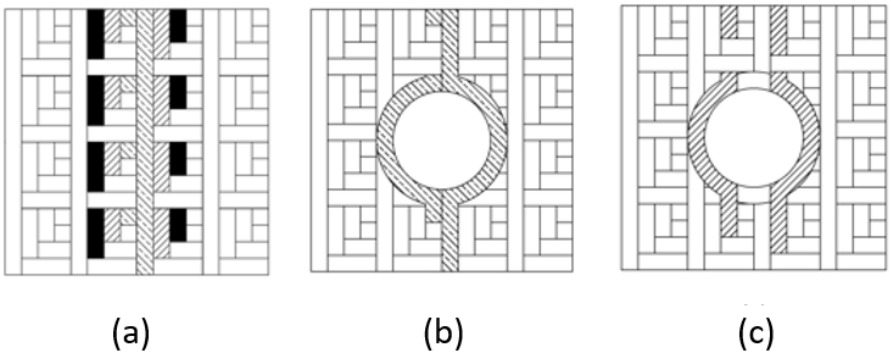

Fig. A. 1. (a) Illustration of warp filaments in a pseudo-woven pattern, showing their alteration due to a through hole, with various infill patterns highlighted (black is the specific fibre tows shown in Fig. 1); (b)-(c) demonstrate how warp filaments are navigated around, apart from those adhering to specific steering patterns. The same principles can be equivalently applied to weft filaments.

For the measurement of the bolt hole dimensions in the specimens, this study employed a vernier calliper with a precision of 0.01 mm. The specific values for each specimen are summarised in Fig. A. 2. It was observed that the bolt hole diameters of the fibre-steered specimens are generally smaller than those of the drilled specimens, which can be attributed to the differences in the fabrication methods. For the fibre-steered specimens, the case involved directly moulding the composite specimens to the desired dimensions

using a mould, with the bolt holes being shaped by a forming pin. Thus, theoretically, during the vacuum bagging process, the melted epoxy would flow and, upon the curing process, solidify to form holes that are approximately the same size as the forming pin. In the fibre-steered process, the epoxy's fluid dynamics and subsequent curing around the forming pin are carefully controlled, leading to a precise replication of the pin's dimensions. This method ensures tight control over the hole's dimensions, often resulting in a slightly smaller bolt hole due to the material compaction around the pin and the minimisation of epoxy shrinkage. Conversely, the mechanical drilling process involves the physical removal of material, which can introduce variations such as drill bit wander or material tearing, potentially resulting in slightly larger holes.

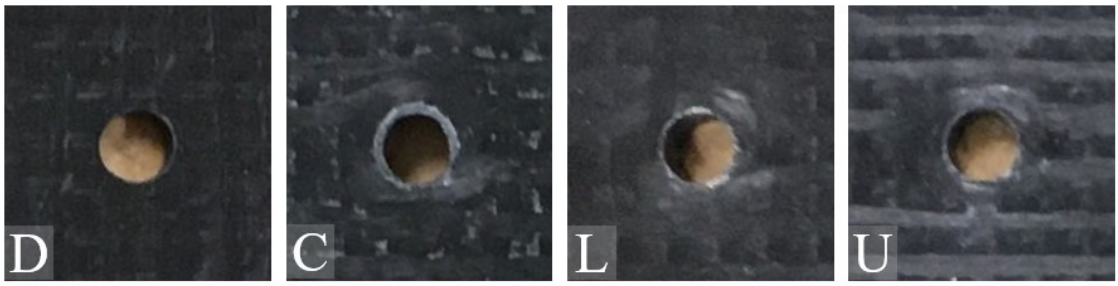

Case	D	C	L	U
Specimen 1	6.01	5.97	5.98	5.99
Specimen 2	6.01	5.99	5.97	5.97
Specimen 3	6.02	6.00	5.96	6.00
Average	6.01	5.99	5.97	5.98

Fig. A. 2. Diagram of representative bolt hole and summary of diameter measurements (mm).

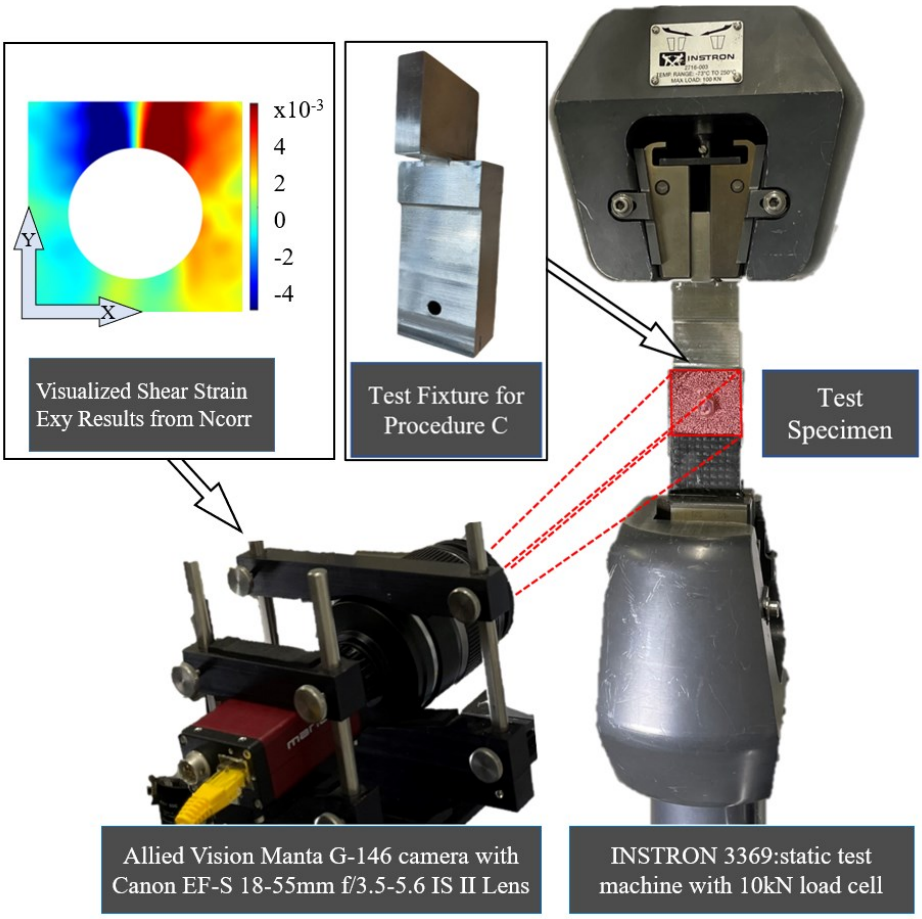

Fig. A. 3 The set-up for procedure C bearing test.

Table A.1 Void content calculated in Avizo

Case	Specimen 1	Specimen 2	Average void content (%)
Mechanically drilled (D)	1.04	1.76	1.40
Squeezed apart (C)	2.47	1.91	2.19
Diverted away (L)	2.79	2.00	2.40
Loop back (U)	2.94	2.48	2.71

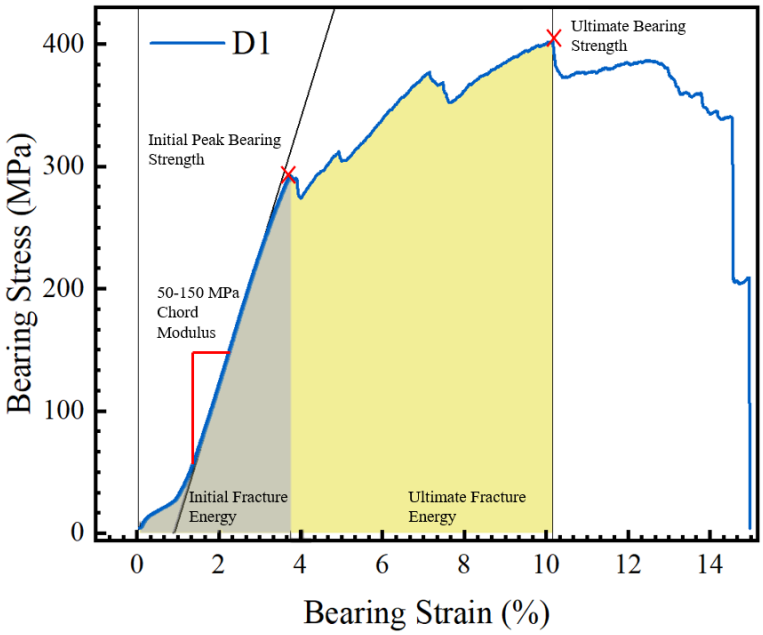

Fig. A. 4 Example (mechanically-drilled hole) of bearing stress/bearing strain curve

The bearing strain, stress and stiffness were calculated according to ASTM-D5961 which is expressed as:

$$F^{br} = \frac{P}{(k * D * h)} \qquad Eq.(A.1)$$

$$\epsilon^{br} = \frac{(\delta_1 + \delta_2)/2}{K * D} \qquad Eq.(A.2)$$

$$E^{\mathrm{br}} = \Delta\,\sigma^{\mathrm{br}} / \Delta\,\varepsilon^{\mathrm{br}} \qquad Eq.(A.3)$$

where *br* refers to bearing, F^{br} is the bearing strength (MPa), P is the load (kN); D is the hole diameter. h is the thickness of the specimen. k is the load per hole factor: 1 for a single fastener test. ϵ^{br} is bearing strain, and δ_1 and δ_2 are displacements of extensometers 1 and 2. In this study, they refer to the displacement of the load cell and the one deduced from DIC by the method mentioned above. K is the factor and 1.0 for double shear. E^{br} is bearing stiffness (GPa), calculated between two specific points in the

essentially linear portion of the load-displacement curve. $\Delta\,\sigma^{br}$ is the change in bearing stress and $\Delta\,\varepsilon^{br}$ is the change in bearing strain.

The initial and ultimate fracture energies were determined by the amount of energy absorbed until the respective points of initial and ultimate failure and were calculated through the integration of the stress-strain curve, as shown in Fig. A. 4 with grey and yellow infill, by using the integrate function in Origin software.

Data availability

Data will be made available on request.

References

[1] Kabir SMF, Mathur K, Seyam A-FM. A critical review on 3D printed continuous fiber-reinforced composites: History, mechanism, materials and properties. Composite Structures. 2020;232.
[2] Simenz RF. The Influence of Aerospace-Performance Requirements on Development of Advanced Structural Materials [and Discussion]. Philosophical Transactions of the Royal Society A: Mathematical, Physical and Engineering Sciences. 1987;322 A(1567):323-33.
[3] Nakamura T, Morino Y, Endo T, Kobayashi M. CFRP application to upper stage structure of Japan's launch vehicles. NASA STI/Recon Technical Report A. 1989;90:923-32.
[4] Quilter A. Composites in aerospace applications. IHS White Paper. 2001;444(1):264.
[5] Li N, Link G, Jelonnek J. 3D microwave printing temperature control of continuous carbon fiber reinforced composites. Composites Science and Technology. 2020;187.
[6] Parandoush P, Lin D. A review on additive manufacturing of polymer-fiber composites. Composite Structures. 2017;182:36-53.
[7] Jenett B, Calisch S, Cellucci D, Cramer N, Gershenfeld N, Swei S, et al. Digital Morphing Wing: Active Wing Shaping Concept Using Composite Lattice-Based Cellular Structures. Soft Robot. 2017;4(1):33-48.
[8] Xu J, Li C, Mi S, An Q, Chen M. Study of drilling-induced defects for CFRP composites using new criteria. Composite Structures. 2018;201:1076-87.
[9] Srinivasa Rao B, Rudramoorthy R, Srinivas S, Nageswara Rao B. Effect of drilling induced damage on notched tensile and pin bearing strengths of woven GFR-epoxy composites. Materials Science and Engineering: A. 2008;472(1-2):347-52.
[10] Eneyew ED, Ramulu M. Experimental study of surface quality and damage when drilling unidirectional CFRP composites. Journal of Materials Research Technology. 2014;3(4):354-62.
[11] Cao Y, Zuo D, Zhao Y, Cao Z, Zhi J, Zheng G, et al. Experimental investigation on bearing behavior and failure mechanism of double-lap thin-ply composite bolted joints. Composite Structures. 2021;261.
[12] McCarthy MA, Lawlor VP, Stanley WF, McCarthy CT. Bolt-hole clearance effects and strength criteria in single-bolt, single-lap, composite bolted joints. Composites Science and Technology. 2002;62(10):1415-31.
[13] Kim BC, Weaver PM, Potter K. Manufacturing characteristics of the continuous tow shearing method for manufacturing of variable angle tow composites. Composites Part A: Applied Science and Manufacturing. 2014;61:141-51.
[14] Frketic J, Dickens T, Ramakrishnan S. Automated manufacturing and processing of fiber-reinforced polymer (FRP) composites: An additive review of contemporary and modern techniques for advanced materials manufacturing. Additive Manufacturing. 2017;14:69-86.
[15] Sano Y, Matsuzaki R, Ueda M, Todoroki A, Hirano Y. 3D printing of discontinuous and continuous fibre composites using stereolithography. Additive Manufacturing. 2018;24:521-7.
[16] Shang J, Tian X, Luo M, Zhu W, Li D, Qin Y, et al. Controllable inter-line bonding performance and fracture patterns of continuous fiber reinforced composites by sinusoidal-path 3D printing. Composites Science and Technology. 2020;192.
[17] Tian X, Liu T, Yang C, Wang Q, Li D. Interface and performance of 3D printed continuous carbon fiber reinforced PLA composites. Composites Part A: Applied Science and Manufacturing. 2016;88:198-205.
[18] Zhang H, Yang D, Sheng Y. Performance-driven 3D printing of continuous curved carbon fibre reinforced polymer composites: A preliminary numerical study. Composites Part B: Engineering. 2018;151:256-64.

[19] Dickson AN, Ross K-A, Dowling DP. Additive manufacturing of woven carbon fibre polymer composites. Composite Structures. 2018;206:637-43.
[20] Zhang H, Dickson AN, Sheng Y, McGrail T, Dowling DP, Wang C, et al. Failure analysis of 3D printed woven composite plates with holes under tensile and shear loading. Composites Part B: Engineering. 2020;186.
[21] Liu T, Tian X, Zhang M, Abliz D, Li D, Ziegmann G. Interfacial performance and fracture patterns of 3D printed continuous carbon fiber with sizing reinforced PA6 composites. Composites Part A: Applied Science and Manufacturing. 2018;114:368-76.
[22] Chacón JM, Caminero MA, Núñez PJ, García-Plaza E, García-Moreno I, Reverte JM. Additive manufacturing of continuous fibre reinforced thermoplastic composites using fused deposition modelling: Effect of process parameters on mechanical properties. Composites Science and Technology. 2019;181:107688.
[23] Swolfs Y, Pinho ST. 3D printed continuous fibre-reinforced composites: Bio-inspired microstructures for improving the translaminar fracture toughness. Composites Science and Technology. 2019;182:107731.
[24] Azarov AV, Antonov FK, Golubev MV, Khaziev AR, Ushanov SA. Composite 3D printing for the small size unmanned aerial vehicle structure. Composites Part B: Engineering. 2019;169:157-63.
[25] Caminero MA, Chacón JM, García-Moreno I, Rodríguez GP. Impact damage resistance of 3D printed continuous fibre reinforced thermoplastic composites using fused deposition modelling. Composites Part B: Engineering. 2018;148:93-103.
[26] Li R, Kelly D, Crosky A. Strength improvement by fibre steering around a pin loaded hole. Composite Structures. 2002;57(1):377-83.
[27] Li R, Kelly D, Crosky A, Schoen H, Smollich L. Improving the Efficiency of Fiber Steered Composite Joints using Load Path Trajectories. Journal of Composite Materials. 2006;40(18):1645-58.
[28] Fujii T, Nakajima K, Iwasaki Y, Osugi Y, Kudo S, Mori N, et al. Application of radial and circular reinforcements for CFRP bolted joints. 21st international conference on composite materials2017.
[29] Sugiyama K, Matsuzaki R, Malakhov AV, Polilov AN, Ueda M, Todoroki A, et al. 3D printing of optimized composites with variable fiber volume fraction and stiffness using continuous fiber. Composites Science and Technology. 2020;186.
[30] Dickson AN, Dowling DP. Enhancing the bearing strength of woven carbon fibre thermoplastic composites through additive manufacturing. Composite Structures. 2019;212:381-8.
[31] Zhang H, Wu J, Robert C, Ó Brádaigh CM, Yang D. 3D printing and epoxy-infusion treatment of curved continuous carbon fibre reinforced dual-polymer composites. Composites Part B: Engineering. 2022;234.
[32] Zhang H, Li A, Wu J, Sun B, Wang C, Yang D. Effectiveness of fibre placement in 3D printed open-hole composites under uniaxial tension. Composites Science and Technology. 2022;220.
[33] Robert C, Pecur T, Maguire JM, Lafferty AD, McCarthy ED, Ó Brádaigh CM. A novel powder-epoxy towpregging line for wind and tidal turbine blades. Composites Part B: Engineering. 2020;203.
[34] Blaber J, Adair B, Antoniou A. Ncorr: Open-Source 2D Digital Image Correlation Matlab Software. Experimental Mechanics. 2015;55(6):1105-22.
[35] Saenz-Castillo D, Martín MI, Calvo S, Rodriguez-Lence F, Güemes A. Effect of processing parameters and void content on mechanical properties and NDI of thermoplastic composites. Composites Part A: Applied Science and Manufacturing. 2019;121:308-20.

[36] Costa ML, De Almeida SfM, Rezende MC. The influence of porosity on the interlaminar shear strength of carbon/epoxy and carbon/bismaleimide fabric laminates. Composites Science and Technology. 2001;61(14):2101-8.
[37] Suhot M, Chambers A. The effects of voids on the flexural properties and failure mechanisms of carbon/epoxy composites. Jurnal Teknologi. 2014;71(2):151-7.
[38] Hernández S, Sket F, González C, Llorca J. Optimization of curing cycle in carbon fiber-reinforced laminates: Void distribution and mechanical properties. Composites Science and Technology. 2013;85:73-82.
[39] Olivier P, Cottu JP, Ferret B. Effects of cure cycle pressure and voids on some mechanical properties of carbon/epoxy laminates. Composites. 1995;26(7):509-15.
[40] Harper B, Staab G, Chen R. A note on the effects of voids upon the hygral and mechanical properties of AS4/3502 graphite/epoxy. Journal of composite materials. 1987;21(3):280-9.
[41] Tang J-M, Lee WI, Springer GS. Effects of Cure Pressure on Resin Flow, Voids, and Mechanical Properties. Journal of Composite Materials. 1987;21(5):421-40.
[42] Yoshida H, Ogasa T, Hayashi R. Statistical approach to the relationship between ILSS and void content of CFRP. Composites Science and Technology. 1986;25(1):3-18.
[43] Hamada H, Coppola J, Hull D. Effect of surface treatment on crushing behaviour of glass cloth/epoxy composite tubes. Composites. 1992;23(2):93-9.
[44] Farley GL. Effect of fiber and matrix maximum strain on the energy absorption of composite materials. Journal of composite materials. 1986;20(4):322-34.
[45] Farley GL, Jones RM. Crushing characteristics of continuous fiber-reinforced composite tubes. Journal of composite Materials. 1992;26(1):37-50.